

The effect of curvature and topology on membrane hydrodynamics

M. L. HENLE¹, R. MCGORTY^{2,3}, A. B. SCHOFIELD⁴, A. D. DINSMORE² and A. J. LEVINE^{1,5}

¹ *Department of Chemistry and Biochemistry, University of California - Los Angeles, CA 90095, USA*

² *Department of Physics, University of Massachusetts - Amherst, MA 01003, USA*

³ *Department of Physics, Harvard University - Cambridge, MA 02138, USA*

⁴ *School of Physics, The University of Edinburgh - Edinburgh EH9 3JZ, UK, EU*

⁵ *California Nanosystems Institute, University of California - Los Angeles, CA 90095, USA*

received 11 July 2008; accepted in final form 5 October 2008

published online 10 November 2008

PACS 87.16.dp – Transport, including channels, pores, and lateral diffusion

PACS 47.63.-b – Biological fluid dynamics

PACS 68.05.-n – Liquid-liquid interfaces

Abstract – We study the mobilities of point-like and extended objects (rods) on a spherical membrane to show how these quantities are modified in a striking manner by the curvature and topology of the membrane. We also present theoretical calculations and experimental measurements of the membrane fluid velocity field around a moving rod bound to the crowded interface of a water-in-oil droplet. By using different droplet sizes, membrane viscosities, and rod lengths, we show that the viscosity mismatch between the interior and exterior fluids leads to a suppression of the fluid flow on small droplets that cannot be captured by the flat-membrane predictions.

Copyright © EPLA, 2008

Introduction. – The dynamics of membrane-bound inclusions is important in many biological and soft matter systems. Mobile inclusions in lipid membranes, such as proteins [1] or lipid “rafts” [2], are fundamental to a variety of biological processes, including signal transduction [3] and the endocytosis of bacterial toxins [4]. Also, the mobilities and hydrodynamic interactions of colloidal particles on crowded fluid-fluid interfaces have ramifications on the design and formation of colloidosomes [5].

Both lipid membrane inclusions and colloidal particles are generically large enough that their motion through the membrane can be treated using continuum hydrodynamics. One can consider the membrane to be a viscous two-dimensional fluid separating two (perhaps dissimilar) solvents and neglect any internal degrees of freedom in the membrane. This description takes into account the distinct nature of the incompressible two-dimensional fluid separating the surrounding solvents. The flows in this fluid can support stresses and thus lead to a discontinuity in the bulk fluid stress across the membrane; furthermore, flows which transport fluid from the membrane to the bulk are not allowed, since the membrane fluid is confined to the surface. This is in marked contrast to an interface between two immiscible fluids, such as oil and water, where the bulk

fluid stress is continuous across the interface and there is no distinct fluid confined there.

The low-Reynolds-number hydrodynamics of viscous membranes differs substantially from the better-known problem of 3D hydrodynamics. The hydrodynamics of an isolated 2D fluid suffers from the same problem as 2D elasticity theory: namely, the response to a point force is log divergent at long length scales [6]. Membrane hydrodynamics, however, is not a purely two-dimensional theory, since flows in the membrane are viscously coupled to flows in the surrounding three-dimensional fluids. This coupling has two principal effects: 1) in-plane momentum in the membrane is not locally conserved, since membrane flows generate bulk fluid flows that transfer momentum out of the membrane; and 2) non-local interactions between points in the membrane, mediated by the flows in the solvents, are generated. The coupling of the membrane to the solvents introduces a new, inherent length scale into membrane hydrodynamics that is unrelated to inertia (*i.e.* Reynolds number). This “Saffman-Delbrück” (SD) length, which is given by the ratio of the (2D) membrane viscosity η_m to the (3D) fluid viscosity η , $\ell_0 \sim \eta_m/\eta$ [7], cuts off the logarithmic divergence mentioned above. For cellular plasma membranes $\ell_0 \simeq 1 \mu\text{m}$ [8]. The existence of

an inherent length scale in membrane hydrodynamics has complex and rather subtle effects on a variety of problems, including protein diffusion in cell membranes [7,9], the flow of monolayers through channels [10], the dynamics of monolayer domains [11], the membrane micro-rheology [12], and the mobilities of both rigid and flexible extended objects in membranes [13].

In this letter, we examine the effects of membrane geometry and topology on membrane hydrodynamics [14]. Specifically, we present both experimental and theoretical results that elucidate these effects on particulate transport in spherical membranes. Our theoretical results show that there are two main effects: first, the spherical topology of the membrane fundamentally alters the membrane velocity field. On a sphere, any non-vanishing vector field must include at least two singularities [15], which can be vortices, sources, or sinks. However, only vortices are allowed for flows on an incompressible membrane, since sources and sinks require compression of the membrane. No such singularities appear on a flat membrane. The compact topology of a spherical membrane also gives rise to an asymmetry between the surrounding 3D fluids that is absent for a flat membrane. Second, the curvature of the membrane introduces a new length scale—the radius of curvature, R —that competes with ℓ_0 in determining the hydrodynamics of particles embedded in the membrane. This length scale acts as a long-distance cutoff in the system, though its unique geometric nature distinguishes it from other long-distance cutoffs in membrane hydrodynamics [7,16,17]. These two effects can exert opposing influences on the transport properties of the membrane. Indeed, their competition results in a particulate mobility that exhibits a surprisingly complex and non-monotonic dependence on the membrane radius.

To experimentally test our theoretical results, we create a two-dimensional colloidal liquid at the spherical interface of a water-in-oil droplet and measure the membrane flow fields created by the motion of a colloidal rod on the membrane. These flow fields show unambiguous deviations from the flat-membrane theory [13] that are consistent with our theoretical predictions for a spherical membrane.

Theoretical model. – Consider a spherical membrane of radius R consisting of a distinct, incompressible fluid of viscosity η_m . We ignore inertial effects and impose force balance at the membrane. We apply a tangential point force $\mathbf{F} = F\hat{y}$ to a rigid disk of radius a at the north pole of the membrane, as illustrated in fig. 1(a). We assume that a is the smallest length scale in the problem, so that we can treat the force on the particle as a point force (we account for the finite particle size via a short-distance cutoff; see below). This force gives rise to an applied force density $\mathbf{f}^{\text{app}} = F\delta(\theta)\hat{y}/(2\pi R^2)$ on the membrane. Because of the curvature of the membrane, the in-plane force balance equation must be written in a manifestly covariant

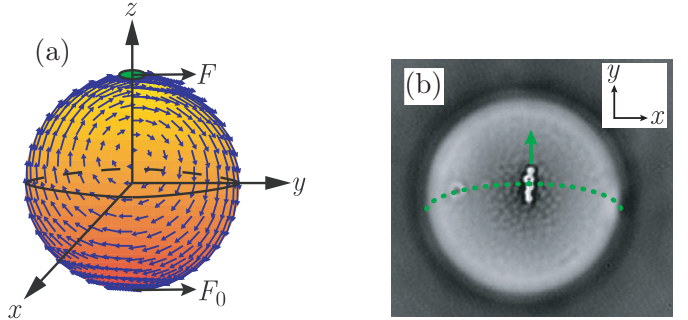


Fig. 1: (Color online) (a) Schematic illustration and calculated membrane velocity field of a point particle of radius a (green disk) at the north pole subject to a force \mathbf{F} , with a pinning force \mathbf{F}_0 at the south pole. Here the interior and exterior fluids are identical: $\eta_+ = \eta_-$, $R/\ell_0 = 0.1$ and $R/a = 100$. (b) Image of a connected rod of paramagnetic spheres at the interface of a water-in-hexadecane droplet decorated with microparticles. The dotted line indicates the line along which the membrane velocity shown in figs. 3 and 4 is measured; the arrow indicates the velocity direction.

form [18]:

$$f_\alpha^{\text{app}} = -\eta_m \left[D^\beta D_\beta v_\alpha + K v_\alpha \right] + \sigma_{\alpha r}^- - \sigma_{\alpha r}^+, \quad (1)$$

where D_α is the covariant derivative and $K = 1/R^2$ is the Gaussian curvature of the sphere; the Greek indices run over the polar and azimuthal angles θ, ϕ , respectively. Here, we have assumed that the membrane is incompressible, $D^\alpha v_\alpha = 0$. The term in brackets in eq. (1) is the viscous force density resulting from gradients in the membrane velocity field v_α ; the last two terms are the viscous stresses due to the solvents inside (σ^-) and outside (σ^+) the spherical surface, $\sigma_{ij}^\pm = \eta_\pm [D_i v_j^\pm + D_j v_i^\pm] - P_\pm \delta_{ij}$, where P_\pm , η_\pm , and \mathbf{v}^\pm are the dynamic pressures, viscosities, and velocities, respectively, of the solvents inside ($-$) and outside ($+$) the sphere. We can see from eq. (1) that geometry can have a dramatic effect on membrane hydrodynamics. In particular, the term $-\eta_m K v_\alpha$ in eq. (1) shows that position-independent flows generate stress in membranes with non-zero Gaussian curvature, such as spheres, but not on membranes with no Gaussian curvature, such as planes and cylinders.

The bulk fluid velocities and pressures satisfy the incompressible Stokes equation: $\nabla^2 \mathbf{v}^\pm = \nabla P_\pm$, $\nabla \cdot \mathbf{v}^\pm = 0$, with boundary conditions $\lim_{r \rightarrow \infty} \mathbf{v}^\pm = \lim_{r \rightarrow 0} \mathbf{v}^\pm = 0$. These boundary conditions in effect provide arbitrary constraint forces that prevent the rigid translation of the membrane and interior fluid. We also impose “stick” boundary conditions at the membrane: $\mathbf{v}^\pm|_{r=R} = \mathbf{v}$.

It is convenient to decompose this dynamical system into normal modes consisting of the combined flows of the membrane and the external solvents. The deformations of a 2D membrane can be decomposed into bending, compression, and shear modes. The incompressibility of the membrane suppresses the compression modes. Thus,

the bending modes are prevented by the incompressibility of the interior fluid, since any bending deformation in the membrane would increase the interior volume of the sphere. The remaining shear modes, which automatically satisfy the membrane incompressibility constraint, can be written as $v_\alpha = \epsilon_{\alpha\beta} D^\beta \Psi$, where $\epsilon_{\alpha\beta}$ is the alternating tensor. The combined membrane and solvent system is diagonalizable in a basis of spherical harmonics [18,19].

By applying the force balance condition eq. (1), we determine the amplitude of each normal mode of the combined membrane/solvent system generated by the applied force. Then the membrane velocity is given by [18]

$$\mathbf{v} \cdot \hat{\theta} = -V \sin \phi \sum_{l=1}^{l_{\max}} \frac{1}{s_l} \csc \theta P_l^1(\cos \theta), \quad (2)$$

$$\mathbf{v} \cdot \hat{\phi} = -V \cos \phi \sum_{l=1}^{l_{\max}} \frac{1}{s_l} [\cot \theta P_l^1(\cos \theta) + P_l^2(\cos \theta)], \quad (3)$$

where $V = F/(4\pi\eta_m)$, l_{\max} is defined below, $P_l^m(x)$ is the l -th associated Legendre function, and

$$s_l = \frac{l(l+1)}{2l+1} \left[l(l+1) - 2 + \frac{R}{\ell_-}(l-1) + \frac{R}{\ell_+}(l+2) \right]. \quad (4)$$

In eq. (4) we have defined two lengths in analogy to the SD length: $\ell_\pm = \eta_m/\eta_\pm$. In contrast, only one length scale, the SD length $\ell_0 \equiv \eta_m/(\eta_- + \eta_+)$, controls the membrane hydrodynamics of a flat membrane. In other words, the viscosities of the two solvents surrounding a flat membrane enter symmetrically, as they must. For a spherical membrane, the asymmetry between the exterior and interior solvents causes these two length scales to enter independently. The most striking manifestation of this asymmetry occurs in the limit of a large interior viscosity, $\eta_- \gg \eta_+$. In that limit eq. (4) shows that the $l=1$ term dominates the sums in eqs. (2) and (3), corresponding to a rigid rotation of the membrane and interior fluid. The opposite limit $\eta_+ \gg \eta_-$ will *not* have an analogous effect. In addition to introducing this asymmetry between the external fluids, we can see from eq. (4) that the geometry of the membrane has another effect: it introduces a new length scale—the membrane radius R —that effectively rescales the SD lengths ℓ_\pm . Indeed, for a small enough sphere, $R \ll \ell_+$, the same rigid body rotation seen in the limit $\eta_- \gg \eta_+$ is observed. Thus, geometry alone can have a dramatic effect on membrane hydrodynamics.

In order to investigate the transport properties of the membrane, we need to isolate the motion of the particle *within* the membrane from the overall motion—specifically, the rigid rotation discussed above—of the entire membrane. To do so, we apply a constraint force \mathbf{F}_0 at the south pole that forces the membrane velocity to vanish there, see fig. 1(a). This force also mimics the adsorption of the membrane onto the substrate in the experiments, see below. Because of the linearity of the Stokes equation, the total response of the fluids is

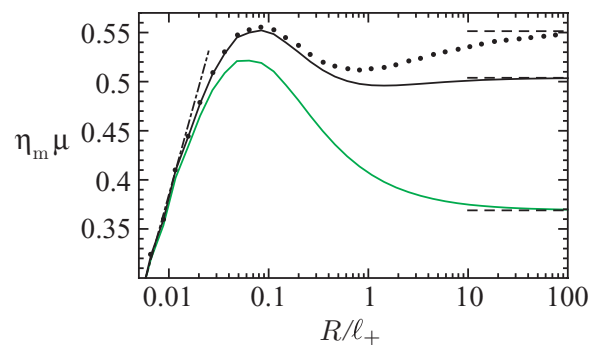


Fig. 2: (Color online) Dimensionless mobility $\eta_m \mu$ for a disk-like particle at the north pole of a pinned spherical membrane as a function of the membrane radius R , for $\ell_+ = 10 \mu\text{m}$, $a = 0.01 \mu\text{m}$, and $\eta_- = 10\eta_+$ (green/gray curve), $\eta_- = \eta_+$ (black curve), or $\eta_- = 0.1\eta_+$ (dotted curve), where η_+ and η_- are the viscosities of the fluids outside and inside the sphere, respectively. The dashed and dot-dashed lines indicate the theoretical asymptotic results (see text).

simply the sum of the individual responses to each force. A typical solution for the membrane velocity field on the sphere is shown in fig. 1(a). The appearance of a vortex in the upper hemisphere is required by topological constraints; there is a similar one placed symmetrically on the back side of the sphere (not shown).

The particle's mobility μ , defined by $\mathbf{v}|_{\theta=0} = \mu \mathbf{F}$, is

$$\mu = \frac{1}{4\pi\eta_m} S_+ \left[1 - \left(\frac{S_-}{S_+} \right)^2 \right], \quad (5)$$

where

$$S_\pm \equiv \sum_{l=1}^{l_{\max}} (\pm 1)^{l+1} \frac{l(l+1)}{2s_l}. \quad (6)$$

The first term in eq. (5) is generated by the force exerted on the particle itself (see eqs. (2) and (3)), while the second term is generated by the pinning force [18]. The finite particle radius a acts as a cutoff, setting the upper limit l_{\max} on the sums in eqs. (2), (3), and (5). In particular, we set the exact value of l_{\max} by requiring that the $R \rightarrow \infty$ limit of eq. (5) agrees with the mobility of a disk of radius $a \ll \ell_0$ in a *flat* membrane [7,9,12]:

$$\mu_{\text{flat}} = \frac{1}{4\pi\eta_m} \ln \left[1 + \frac{2\ell_0}{a} e^{-\gamma} \right], \quad (7)$$

where γ is Euler's constant. It is straightforward to show that eq. (5) has the correct limiting behavior if we set l_{\max} equal to the largest integer less than $2e^{-\gamma}R/a$.

Figure 2 shows the dimensionless mobility $\eta_m \mu$ of a particle at the north pole of a pinned spherical membrane as a function of R for a variety of interior viscosities η_- . As expected, the flat-membrane SD result eq. (7) (horizontal dashed lines) is recovered in the limit $R \rightarrow \infty$ in all cases. The approach to this limit, however, is dependent on the viscosity ratio η_+/η_- . For $\eta_+/\eta_- < 1$ (green/gray curve), the mobility in a spherical membrane is larger than in

a flat membrane because here the more viscous fluid is bounded, causing it to dissipate less energy. Conversely, when $\eta_+/\eta_- > 1$ (dotted curve), the mobility in a spherical membrane is suppressed relative to the flat case.

In the limit of high membrane curvature, $R/\ell_+ \ll 1$, $\eta_m \mu \rightarrow \ln(R/a)/2\pi$ (dot-dashed line). The appearance of R as the long-distance cutoff in the logarithm is generally expected [7,16,17], but the prefactor is determined by the spherical geometry. Hence, particle mobilities in high-curvature membranes, $R/\ell_+ \ll 1$, are depressed relative to the SD result.

For intermediate curvatures, the mobility exhibits an interesting non-monotonic behavior on the particle radius. In particular, there is a clear maximum in the mobility for moderately small values of R/ℓ_+ , independent of the viscosity ratio η_+/η_- . In contrast, the corresponding mobilities on a *cylindrical* membrane exhibit no such peaks [18]. Therefore, this maximum is a striking illustration of the effects of the *geometry* of the sphere on the transport properties of the membrane. In particular, the presence of the Gaussian curvature term in the force balance equation (1) alters the mobility for membranes with non-zero Gaussian curvature. The different roles of topology and geometry in membrane hydrodynamics will be investigated further in a future publication [18].

We now turn to the problem of the mobility of, and fluid flows around, extended objects embedded in the membrane. Specifically, we consider a rod of length L embedded in the membrane. Using the Kirkwood approximation [20], we model the rod as a linear array of $N + 1$ disks of radius a separated by a distance b , where $L = Nb + 2a$. We also apply a pinning force at the south pole. Using the superposition principle, the total membrane velocity is $v_\alpha^{\text{tot}}(\theta, \phi) = \sum_{i=0}^{N+1} F_\beta^{(i)} \chi_{\alpha,\beta}(\theta, \phi; \theta_i, \phi_i)$. Here, $\mathbf{F}^{(i)}$ is the force applied to the disk at the point (θ_i, ϕ_i) ; $i = 0$ corresponds to the south pole, and $i = 1, \dots, N + 1$ labels the disks in the rod. We choose our coordinate system so that the rod lies along the great circle $\phi = \pi/2$ of the sphere with its center at the north pole, so that $\theta_i = \frac{b}{R}|\frac{N}{2} + 1 - i|$ for $i \neq 0$. We consider only forces parallel to the rod axis. The response function $\chi_{\alpha,\beta}(\mathbf{x}; \mathbf{y})$ gives $v_\alpha(\mathbf{x})$ due to a unit force in the β -direction applied at \mathbf{y} .

To determine the forces $\mathbf{F}^{(i)}$, we require the total fluid velocity to vanish at the south pole and each disk in the rod to move with unit velocity. These constraints provide a set of $N + 2$ linear equations that determine $\mathbf{F}^{(i)}$. Summing the $N + 1$ forces acting on the rod moving at unit velocity gives the inverse mobility of the rod. Using these forces, we can determine the entire velocity field in response to the rod's motion, both on the sphere and in the surrounding fluids.

In fig. 3, we plot the membrane velocity field $\mathbf{v}_\perp = v_\perp(\theta)\hat{\mathbf{y}}$ along the line that perpendicularly bisects the rod (*i.e.* the line $\phi = 0, \pi$, $0 < \theta < \pi$ —see fig. 1(b)), as a function of the polar angle θ , for various values of the membrane radius R (black, green, and dashed curves). For comparison, we also plot a projection of the flat-membrane

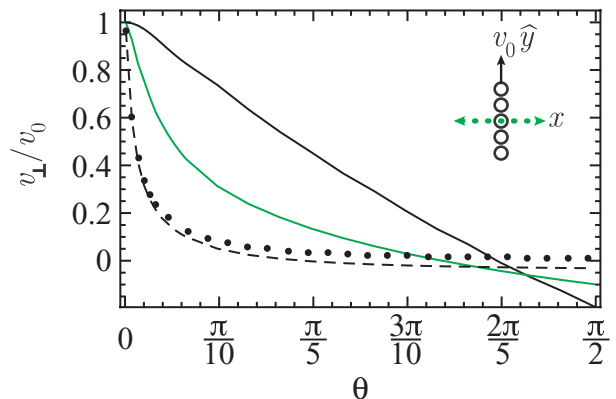


Fig. 3: (Color online) membrane velocity v_\perp surrounding a membrane-bound rod of length $L = 2 \mu\text{m}$, measured along the axis indicated by the dotted line in the schematic illustration (inset), as a function of the polar angle θ for various values of the membrane radius R . For all curves, $a = 0.1 \mu\text{m}$, $\ell_+ = \ell_- = 20 \mu\text{m}$, $b = 2a$, and $N = 9$; the membrane radii are $R = 2 \mu\text{m}$ (black curve), $R = 10 \mu\text{m}$ (green/gray curve), and $R = 50 \mu\text{m}$ (dashed curve). We also show the flat-membrane result (dotted curve), which has been mapped onto the largest sphere using the arc-length $R\theta$ as the flat-space distance.

result [12] onto the largest sphere (dotted curve); that is, we map the flat-plane distance d onto an angle θ using the arc-length $R\theta$ of the largest sphere. We can see that when the sphere is large, the membrane velocity field near the rod approaches the flat-membrane result. However, at large angles the velocity field on the sphere is negative, indicating the presence of a vortex (see fig. 1(a)). No such vortex exists on the flat membrane, where the velocity field decreases monotonically to zero. As the radius of the sphere is decreased, a dramatic change in the membrane velocity field occurs: the velocity field gradients decrease, causing the vortex to migrate towards the equator. The principal effect of curvature on the spatial structure of the flow fields around a moving particle can be understood in terms of the rescaling of the SD lengths ℓ_\pm by the membrane radius R (see eq. (4)), as long as $R/a \gg 1$. Therefore, we expect that a higher curvature generates flow fields corresponding to a membrane with a larger effective viscosity η_m , *i.e.* flow fields with smaller spatial gradients, which is precisely the behavior shown in fig. 3.

Experiments. — To test our model, we performed experiments to measure the flow fields on spherical droplets caused by the motion of a rod-like object confined to the droplet surface. Water droplets ($\eta_- = 10^{-3} \text{ N s/m}^2$), typically 30–100 μm in diameter, suspended in hexadecane ($\eta_+ = 3.34 \times 10^{-3} \text{ N s/m}^2$) provided the spherical interface. The interface was coated with a monolayer of small (370 nm diameter, measured by scanning electron microscopy) poly(methyl methacrylate) (PMMA) spheres, which were sterically stabilized by poly(hydroxystearic acid) and labeled with NBD fluorescent dye (7-chloro-4-nitrobenzofurazan) [21]. This monolayer is confined to

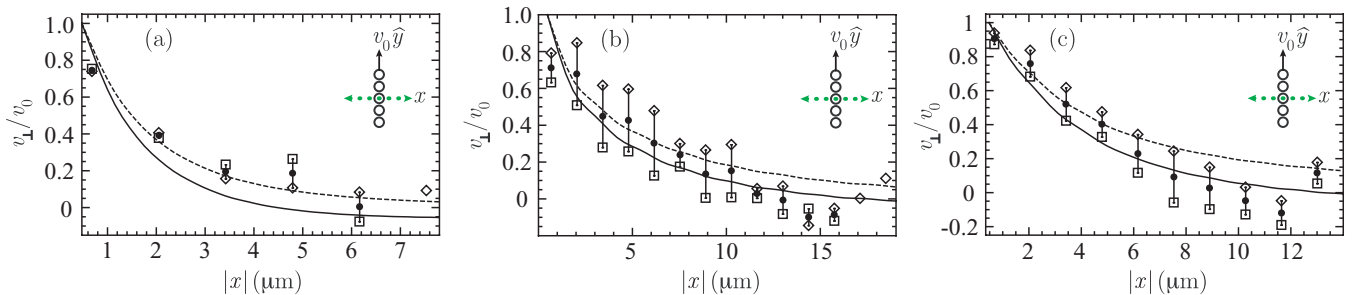


Fig. 4: (Color online) Experimental data (points) and theoretical predictions (lines) for the membrane velocity v_{\perp} measured along the axis indicated by the dotted line in the schematic illustration (upper right-hand corner of each panel). The open squares (diamonds) correspond to data on the right (left) side of the rod, *i.e.* $x > 0$ ($x < 0$); the solid circles are the mean of these two points. The solid lines show the predictions of the spherical membrane theory (SMT), while the dashed lines show those of the flat-membrane theory (FMT) [13]. The theoretical curves were generated using the parameters: (a) $\ell_0 = 0.22 \mu\text{m}$ (SMT), $\ell_0 = 0.25 \mu\text{m}$ (FMT), $L = 6.4 \mu\text{m}$, $R = 17.5 \mu\text{m}$, $N = 30$. This data corresponds to fig. 1(b); (b) $\ell_0 = 0.46 \mu\text{m}$ (SMT), $\ell_0 = 0.48 \mu\text{m}$ (FMT), $L = 31.6 \mu\text{m}$, $R = 54 \mu\text{m}$, $N = 35$; (c) $\ell_0 = 7.32 \mu\text{m}$ (SMT), $\ell_0 = 8.12 \mu\text{m}$ (FMT), $L = 7 \mu\text{m}$, $R = 26 \mu\text{m}$, $N = 10$.

the interface [22], effectively creating a distinct membrane fluid there. The PMMA particles served dual roles: to set the membrane viscosity and to allow measurement of the membrane flow field using video microscopy and particle-tracking software. Spheres were imaged using bright-field optical microscopy (not fluorescence) using a Zeiss Axiovert 200 with a $100\times$ objective and a numerical aperture equal to 1.3. Images were captured at 30 frames/s and analyzed with particle-tracking code written in IDL [23]. A representative image is shown in fig. 1(b). Finally, the glass coverslips were treated with dichlorodimethylsilane before the experiments to prevent wetting of the water droplet on the glass. During the measurements, the droplets lay on the bottom of the viewing cell and the PMMA particles at the bottom of the droplet adhered to the coverslip, preventing the rotation of the droplet as a whole.

To create the rod, we added paramagnetic polystyrene spheres that adsorbed to the interface. These $0.95 \mu\text{m}$ diameter spheres were made of carboxylate-functionalized, divinylbenzene- (DVB-) crosslinked polystyrene containing iron oxide (Bangs Laboratories item # MC04N, lot 3251). In the presence of a magnetic field, the spheres aligned into a single rod-shaped aggregate, see fig. 1(b). The rod was moved at speeds of approximately a few $\mu\text{m/s}$ along the surface by a permanent magnet brought close to the sample. To measure the flow field, $\mathcal{O}(10^2)$ PMMA particles were tracked during the rod's motion. For each droplet, the process was typically repeated twelve times, and the mean and statistical uncertainty of the flow velocities were measured. Droplets of different radii, rod lengths, and viscosities were used.

In fig. 4 we plot the measured membrane velocity (open points) along the line that perpendicularly bisects the rod—that is, the velocity \mathbf{v}_{\perp} plotted in fig. 3—as a function of the absolute distance $|x| = R|\sin\theta|$ from the north pole in the $\hat{\mathbf{x}}$ -direction. By symmetry, we expect the velocity field to be symmetric about the rod axis. However, as shown in fig. 4, the data can exhibit asymmetries

due to random experimental error and asymmetries in the colloidal suspension. Therefore, to compare with the theoretical predictions we indicate the average velocity value by the solid points.

To generate the theoretical velocity profiles for these measurements, we need to determine the membrane viscosity η_m , which in turn sets the value of ℓ_0 . To do so, the positions r of the PMMA spheres were measured as they underwent thermal motion on the surface of the droplet (*i.e.* in the absence of any applied forces). A typical set of measurements tracked 40 particles over a total period of 20–40 s. The mean-square displacements, $\langle [r(t-t_0) - r(t_0)]^2 \rangle \equiv \Delta r^2(t)$, were computed by averaging over all PMMA spheres and all times t_0 . The slope of $\Delta r^2(t)$ in the linear (long-time) regime was measured, and the diffusion constant D was obtained from the relation $\Delta r^2(t) = 4Dt$. For the three samples shown in fig. 4, we obtained the following diffusion constants D : (a) $0.28 \mu\text{m}^2/\text{s}$; (b) $0.21 \mu\text{m}^2/\text{s}$; and (c) $0.037 \mu\text{m}^2/\text{s}$. Using these values for D , the Saffman-Delbrück length ℓ_0 for each sample was determined from the Stokes-Einstein relation $D = k_B T \mu$ and the mobility of a point-like particle in a membrane. For a spherical membrane, this mobility is given by eq. (5); for a flat membrane, it is given by eq. (7).

In figs. 4(a)–(c), we show a sequence of droplets demonstrating the increasing effect of curvature. We show the predictions of the flat-membrane theory (FMT, dashed lines) [13] and the spherical membrane theory (SMT, solid lines); each curve is obtained by direct calculation using no adjustable parameters. We account for the rod thickness in the theory by setting v_{\perp} equal to the rod velocity v_0 everywhere within the rod. The substrate pins the fluid velocity at the south pole (we do not account for any additional hydrodynamic interactions between the sphere and the substrate). In fig. 4(a), where $R \gg \ell_0$, we see that both the FMT and SMT are close to the data. In fig. 4(b), where $R \gg \ell_0$, but is now comparable to L , the

effects of curvature begin to be seen. However, only when ℓ_0 approaches R , as in fig. 4(c), does the effect of curvature become dramatic. Here the velocity field decays more rapidly away from the rod than the FMT predictions. In this case the SMT prediction is a significant improvement over that of the FMT. This is in marked contrast to the behavior shown in fig. 3, where the velocity field exhibits *smaller* gradients as the curvature is increased. However, that behavior is seen in the limit $R/\ell_+ \ll 1$, whereas for all the data in fig. 4 the droplet radii R are larger than the SD lengths ℓ_{\pm} . We can understand the suppression of the velocity fields in fig. 4 by first considering the case in which the interior viscosity is much larger than the exterior viscosity. In this case, large gradients in the velocity field of the interior fluid are suppressed. These nearly spatially homogeneous flows generate large gradients in the velocity field of the exterior fluid. This is seen most clearly when the membrane and interior fluid rotate as a rigid object, where all of the dissipative flows occur in the exterior fluid. When the situation is reversed—that is, when the interior fluid is *less* viscous—the flows of the membrane and interior fluid become more localized around the rod in order to minimize long-range flow in the more viscous exterior fluid. Thus, the viscosity mismatch between the less viscous interior fluid (water) and the more viscous exterior fluid (oil) enhances the localization of the membrane velocity field around the rod, as seen in fig. 4(c).

Conclusion. — This work demonstrates the considerable effect of membrane curvature and topology on the transport of particles embedded in the membrane. The compact topology of the sphere requires the formation of vortices in steady-state, zero-Reynolds-number flow; it also implies an asymmetry between the interior and exterior solvents, which can enhance or suppress particulate transport relative to that of a flat membrane. Furthermore, the diffusivity of particles bound to membranes of high curvature is significantly reduced. The experimental data, while somewhat noisy, do show a decay in the velocity field away from the rod that is faster than the FMT predictions and consistent with the SMT. The conclusions of this work should be relevant to understanding the kinetics of particulate aggregates on the surface of droplets and the transport of proteins on membranes separating the viscous cytosol from extracellular fluids.

AJL thanks T. LIVERPOOL for enjoyable and enlightening discussions. MLH and AJL were supported in part by NASA NRA 02-OBPR-03-C. ADD acknowledges support through a Faculty Research Grant from the University of Massachusetts, Amherst. ADD and RM thank KAN DU and the microscopy facilities of the NSF-funded UMass Materials Research Science and Engineering Center on Polymers for technical assistance.

REFERENCES

- [1] REITS E. A. J. and NEEFJES J. J., *Nat. Cell Biol.*, **3** (2001) E145.
- [2] MAXFIELD F. R. and TABAS I., *Nature*, **438** (2005) 612.
- [3] SCHLESSINGER J., *Cell*, **110** (2002) 669; DUNHAM S. M. *et al.*, *J. Phys. Chem. B*, **108** (2004) 10540.
- [4] ABRAMI L. *et al.*, *J. Cell. Biol.*, **60** (2003) 321.
- [5] DINSMORE A. D. *et al.*, *Science*, **298** (2002) 1006; LIN Y. *et al.*, *Langmuir*, **21** (2005) 191; ZENG C., BISSIG H. and DINSMORE A. D., *Solid State Commun.*, **139** (2006) 547; ZHENG L. and GRANICK S., *Nano Lett.*, **6** (2006) 694.
- [6] CHAIKIN P. M. and LUBENSKY T. C., *Principles of Condensed Matter Physics* (Cambridge University Press, Cambridge) 1995.
- [7] SAFFMAN P. G. and DELBRÜCK M., *Proc. Natl. Acad. Sci. U.S.A.*, **72** (1975) 3111; STONE H. A. and AJDARI A., *J. Fluid Mech.*, **369** (1998) 151; STONE H. A., *J. Fluid Mech.*, **409** (2000) 165.
- [8] PINAUD F., PhD Thesis, UCLA (2007).
- [9] HUGHES B. D., PAILTHROPE B. A. and WHITE L. R., *J. Fluid Mech.*, **110** (1981) 349.
- [10] SCHWARTZ D. K., KNOBLER C. M. and BRUINSMA R., *Phys. Rev. Lett.*, **73** (1994) 2841; STONE H. A., *Phys. Fluids*, **7** (1995) 2931.
- [11] STONE H. A. and MCCONNELL H. M., *Proc. R. Soc. London, Ser. A*, **448** (1995) 97; *J. Phys. Chem.*, **99** (1995) 13505; LUBENSKY D. K. and GOLDSTEIN R. E., *Phys. Fluids*, **8** (1996) 843.
- [12] LEVINE A. J. and MACKINTOSH F. C., *Phys. Rev. E*, **66** (2002) 061606; PRASAD V., KOEHLER S. A. and WEEKS E. R., *Phys. Rev. Lett.*, **97** (2006) 176001; ANGUELOUCH A., LEHENY R. L. and REICH D. H., *Appl. Phys. Lett.*, **89** (2006) 111914; SICKERT M., RONDELEZ F. and STONE H. A., *EPL*, **79** (2007) 66005.
- [13] LEVINE A. J., LIVERPOOL T. B. and MACKINTOSH F. C., *Phys. Rev. E*, **69** (2004) 021503; *Phys. Rev. Lett.*, **93** (2004) 038102.
- [14] CAI W. and LUBENSKY T. C., *Phys. Rev. E*, **52** (1995) 4251; SEIFERT U., *Eur. Phys. J. B*, **8** (1999) 405; MIAO L., LOMHOLT M. A. and KLEIS J., *Eur. Phys. J. E*, **9** (2002) 143; LOMHOLT M. A., HANSEN P. L. and MIAO L., *Eur. Phys. J. E*, **16** (2005) 439; HU D., ZHANG P. and E W., *Phys. Rev. E*, **75** (2007) 041605.
- [15] MILNOR J., *Topology from the Differentiable Viewpoint, Princeton Landmarks in Mathematics* (Princeton University Press, Princeton) 1965.
- [16] DANIELS D. R. and TURNER M. S., *Langmuir*, **23** (2007) 6667.
- [17] EVANS E. and SACKMANN E., *J. Fluid Mech.*, **194** (1988) 553.
- [18] HENLE M. L. and LEVINE A. J., in preparation.
- [19] HAPPEL J. and BRENNER H., *Low Reynolds Number Hydrodynamics* (Kluwer, Boston) 1983.
- [20] KIRKWOOD J. G. and RISEMAN J., *J. Chem. Phys.*, **16** (1948) 565.
- [21] JARDINE R. S. and BARTLETT P., *Colloid Surf. A: Physicochem. Eng. Aspects*, **211** (2002) 127.
- [22] PIERANSKI P., *Phys. Rev. Lett.*, **45** (1980) 569.
- [23] CROCKER J. C. and GRIER D. G., *J. Colloid Interface Sci.*, **179** (1996) 298.